JTTEES 7:527-536

PEER REVIEWED

Comparison of Plasma-Sprayed Coatings Produced in Argon or Nitrogen Atmosphere

M. Leylavergne, B. Dussoubs, A. Vardelle, and N. Goubot

(Submitted 26 February 1998; in revised form 12 May 1998)

When spraying is conducted at ambient atmosphere, the entrainment of air cools the plasma jet and affects its expansion. It can also cause oxidation or chemical decomposition of the sprayed materials. Inert plasma spraying (IPS), generally conducted in an argon atmosphere, prevents these phenomena. However, the main drawbacks of IPS in comparison with air plasma spraying are the capital and operating costs. This paper presents a study in which nitrogen is used as a substitute for conventional argon atmosphere, thus reducing costs by 25 to 30%. Titanium carbide and niobium powders were sprayed in both argon and nitrogen atmospheres. Cryogenic cooling of the substrate was used during the spray process. This helps to maintain a low temperature in the chamber, produce thick coatings, and allows the use of substrate materials that are sensitive to heat.

The velocity, temperature, and composition fields of the argon-hydrogen plasma jet flowing in argon or nitrogen at atmospheric pressure are compared from numerical simulation. The adhesion, roughness, and microstructure of the niobium and TiC coatings produced in both atmospheres are discussed as well as their nitrogen content.

Keywords argon atmosphere, coating analysis, gas dynamics modeling, inert plasma spraying, nitrogen atmosphere

1. Introduction

In the air plasma spray (APS) process, the mixing of the plasma jet with the ambient atmosphere affects the plasma flow (Ref 1-3). This results in an efficient cooling and slowing of the jet.

The mixing with air can also alter the chemical composition of the jet and affect the heat and mass transfer to particles, as well as coating properties. The presence of oxygen can result in oxidation of metallic particles or favor a chemical decomposition; these phenomena can occur during the flight of the particle or after impact of the droplet on the substrate (Ref 4). In addition, the presence of oxygen in the gaseous boundary layer around the particle increases their rate of vaporization. Indeed, because the oxygen atoms react with the vapor, the homogeneous reaction consumes the metal atoms, and the decrease in the metal vapor pressure around the droplets enhances the rate of volatilization from the liquid surface (Ref 5).

To minimize the oxidation or chemical decomposition, the powders can be sprayed in a controlled atmosphere, for example, an argon atmosphere. However, this inert plasma spray (IPS) process requires considerable capital cost and running expenses, especially when argon cryogenic cooling is used. The latter makes it possible to keep the substrate at a low temperature. It allows the use of materials sensitive to heat as substrate materials and the production of thick coatings by reducing the residual stresses due to the mismatch of the expansion coefficient of the substrate and the coating. Moreover, cryogenic cooling enables control of the temperature inside the chamber and protects the material handling system from excessive heating.

To reduce the coating production cost by 25 to 30%, a nitrogen atmosphere can be used as a substitute for the conventional argon atmosphere. The objective of this study is to compare IPS when using argon and nitrogen atmospheres with various powders sprayed on graphite substrates with an Ar-H_2 plasma jet and cryogenic cooling of the substrate. In this paper, titanium carbide and niobium coatings are addressed. The mixing of the plasma jet with the argon and nitrogen, and the way this affects flow temperature and velocity, are studied using a computational fluid dynamics model. The microstructure and nitrogen content of coatings are analyzed as well as their adhesion, roughness, and hardness.

M. Leylavergne and **A.Vardelle,** ENSIL, Parc d'Ester Technopôle, 87068 Limoges, France; **B. Dussoubs,** LMCTS, University of Limoges, 123 Avenue A. Thomas, 87060 Limoges Cedex, France; and **N. Goubot,** CEA/Valrho, BP111, Pierrelatte, France. Contact A. Vardelle at e-mail: armelle@ensil.unilim.fr.

2. Experimental Procedure

2.1 Experimental Setup

The plasma torch was a SNMI (Société Nouvelle de Métallisation Industrielle, Avignon, France) gun with an inside nozzle diameter of 8 mm. The plasma-forming gas consisted of a mixture of argon and hydrogen. Powder was injected through a 1.7 mm diameter port located 2.2 mm from the nozzle exit. The stand-off distance between the front face of the torch and the substrate was 100 mm. Table 1 lists the torch operating conditions used in this study. Coatings were produced with cryogenic cooling of the substrate. The cryogenic system consisted of four nozzles located 40 mm upstream of the substrate. The liquid argon or nitrogen issuing from these nozzles were broken into fine droplets by argon or nitrogen gas jets. The purity of argon and nitrogen used as plasma-forming gas and for substrate cooling were 99.995 and 99.997%, respectively. The temperature of the substrate was measured by a thermocouple and controlled at approximately 150 °C during the spray process. Figure 1 shows a schematic view of the experimental setup.

Nomenclature

A_{ij} Coefficients of the Mason and Saxena formula
Bi Biot number, $Bi = \frac{\kappa_f}{\kappa_p}$
C_P Specific heat, $J \cdot kg^{-1} \cdot °C^{-1}$
d Diameter, m
D Species diffusivity, $m^2 \cdot s^{-1}$
$\mathbf{f}$ Vector representing all the forces applied to a unit mass of fluid, $N \cdot kg^{-1}$
h Heat transfer coefficient, $W \cdot m^{-2} \cdot °C^{-1}$
H Mass enthalpy, $J \cdot kg^{-1}$
k Kinetic turbulent energy, $m^2 \cdot s^{-2}$
m Mass fraction
M Molecular weight, $kg \cdot mol^{-1}$
Nu Nusselt number, $\nu = \frac{hd_P}{\kappa_f}$
p Pressure, Pa
Pr Prandtl number, $Pr = \frac{\mu_f C_{P,f}}{\kappa_f}$
Q_m Mass flow rate, $kg \cdot s^{-1}$
r Radius, m
R Radius of the nozzle, m
Re Reynolds number, $Re = \frac{\rho_f V_r d}{\mu_f}$
Rm Parameter characterizing the effect of the transverse injection of a cold gas in the jet
S Source term, variable
Sc Schmidt number, $Sc = \frac{\mu_f}{\rho_f D}$
t Time, s
T Temperature, °C
$\mathbf{V}$ Velocity vector of components u, v, and w in the Cartesian frame x,y,z, $m \cdot s^{-1}$
$\mathbf{V_r}$ Relative velocity between the gas and the particle, $m \cdot s^{-1}$
x Molar fraction

Greek Symbols

β Ratio of atomic lines
Γ Transport coefficient, $kg \cdot m^{-1} \cdot s^{-1}$
ΔH Specific heat, $J \cdot kg^{-1}$
ε Dissipation rate of turbulent energy, $m^2 \cdot s^{-3}$
φ Variable
φ_{ij} Coefficients of the Wilke formula
κ Thermal conductivity, $W \cdot m^{-1} \cdot °C^{-1}$
μ Dynamic viscosity, $kg \cdot m^{-1} \cdot s^{-1}$
ρ Density, $kg \cdot m^{-3}$

Subscripts

0 At time $t = 0$
a Anode
eff Effective
f Plasma flow
h Enthalpy
i Relative to the ith species
inj Injection
m Maximum, on centerline
me Melting
p Particle
r Relative to particle residence time
t Turbulent

The results reported in this paper are related to niobium and titanium carbide powders supplied by HC Starck. Figure 2 shows their morphology, and their thermophysical properties are listed in Table 2. The particle size distribution of the powders was measured using a laser Malvern 2600C particle sizer. The scanning electron microscopy pictures of the powders showed that the niobium particles exhibited an angular shape and rather uniform size (mean diameter = 100 μm), while the titanium carbide powder contained a large number of small particles (mean diameter = 25 μm). Table 3 sums up the size distribution and chemical content of these powders. The chemical content was determined using Rosemount CSA 5003 and NOA 5003 analyzers.

The coatings were deposited on graphite substrates (160 by 75 by 10 mm), which were sand blasted just before deposition. The mass deposition efficiency of the process was determined by spraying on 0.5 mm steel substrates.

2.2 Coating Analyses and Testing

The coatings were analyzed after the spray process and after a 10 h heat treatment period at 1250 °C under 10 Pa. The heating and cooling rates for this experiment were 3.3×10^{-2} °C · s^{-1}.

Table 1 Spray parameters

Powders	Nb	TiC
Argon flow rate, slm	47	47
Hydrogen flow rate, slm	9	12
Arc voltage, V	77	80
Arc current, A	470	593
Effective arc power, kW	19.5	22.0
Carrier gas flow rate, slm	10	10
Powder feed rate, $kg \cdot s^{-1}$	$3.5 \cdot 10^{-4}$	$3.3 \cdot 10^{-4}$
Stand-off distance, mm	100	100

Table 2 Physical properties of the sprayed materials

Physical properties	Nb	TiC
Density, $kg \cdot m^{-3}$	8570	4930
Melting point, °C	2468	3140
Thermal conductivity at 25 °C, $W \cdot m^{-1} \cdot °C^{-1}$	53	21
Thermal expansion at 25 °C, 10^{-6} °C^{-1}	7.3	7.7
Specific heat at 25 °C, $J \cdot mol^{-1} \cdot °C^{-1}$	24.8	33.8

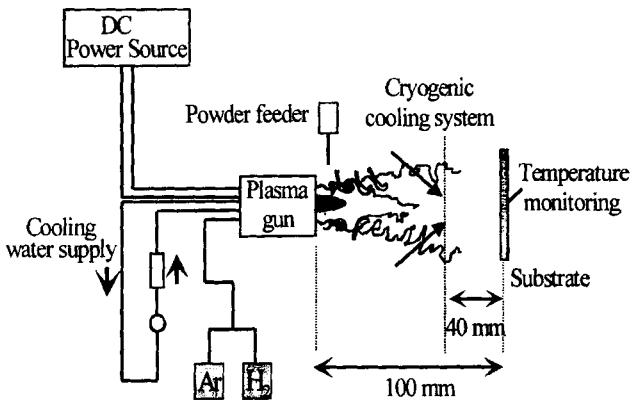

Fig. 1 Schematic view of the experimental setup

The cross-section microstructures of the coatings were observed through scanning electron microscopy of the polished surfaces. The adhesive strengths of the coatings were measured by determining the maximum tensile load required to separate the coating from its substrate. Samples of $4 \cdot 10^{-4}$ m^2 were bonded on supports of identical section using Araldite AW 2101 glue and HW 2951 hardener supplied by SODIEMA. The traction apparatus measured loads between 2 and 20,000 N, and the displacement speed was fixed at $3.3\ 10^{-5}$ m $\cdot$ s^{-1}. Five samples were tested for each coating. Microhardness measurements were conducted on polished cross sections using a Vickers indentor at 0.5 N for TiC coatings and 0.25 N for niobium coatings. For each sample, ten roughness profiles 32 mm long were analyzed by a SURFASCAN two-dimensional apparatus to determine surface roughness (R_a) and total roughness (R_t). The phase content of the coatings was examined using x-ray diffraction. The nitrogen and oxygen contents were determined with a Rosemount NOA 5003 analyzer and the total carbon content with a Rosemount CSA 5003 analyzer. Raman spectroscopy was also used to characterize niobium coatings.

3. Mathematical Model

3.1 Gas Dynamics Modeling

The modeling of the plasma jet and its mixing with the surrounding atmosphere was carried out using a commercial fluid dynamics program: ESTET (Ref 6, 7). This three-dimensional package solves the conservation equations of mass, momentum, and energy for expansible, compressible, and turbulent flows.

The numerical simulation was based on the following assumptions: (a) the plasma flow was turbulent, except within the potential core, (b) the system was steady and in local thermodynamic equilibrium (LTE), (c) the plasma was optically thin, and (d) no chemical reaction or demixing occurred in the gas phase.

The conservation equations for the gas phase were written in the general form:

$$\mathrm{div}(\rho\varphi\mathbf{V}) = \mathrm{div}[\Gamma_\varphi \mathbf{grad}(\varphi)] + S_\varphi \qquad \text{(Eq 1)}$$

where ρ is the mass density of the mixture, φ is a variable, $\mathbf{V}$ is the velocity vector, and Γ_φ and S_φ are the transport coefficient and the source term relative to the variable φ, respectively. Bold characters in Eq 1 indicate vectors. Table 4 summarizes for each variable φ, the corresponding transport coefficient Γ_φ and the source term S_φ. In this table, p corresponds to the pressure; $\mathbf{f}_x$, $\mathbf{f}_y$, $\mathbf{f}_z$ are the components of the volumetric force vector; $\mathbf{u}$, $\mathbf{v}$, and $\mathbf{w}$ are the components of the velocity vector; and μ, κ, and C_p are the viscosity, the thermal conductivity, and the specific heat of the gas, respectively. Pr_t is the turbulent Prandtl number, X_i and D_i are the volume fraction and the diffusion coefficient of the ith species, respectively, Sc_t is the turbulent Schmidt number, and k and ε are the turbulent kinetic energy and the dissipation of the kinetic energy.

Table 3 Size distribution and chemical analysis of the powders used in this study

Powder type	Nb, fused and crushed	TiC, sintered
Size distribution		
$D_{50\%}$, μm	100	25
$D_{90\%}$, μm	156	46
$D_{10\%}$, μm	72	12
Chemical contents		
C, wt%	0.003	19.2
O, wt%	0.06	0.12
N, wt%	0.006	0.14

The standard k-ε turbulence model of Launder and Spalding (Ref 8) was used along with the correction of Launder and Sharma (Ref 9) for low Reynolds numbers, which applied in the potential core of the jet and close to the walls. The standard values, given in Table 5, were used for the constants of the k-ε model.

In the ESTET code, the species diffusion is assumed to be similar to heat diffusion; that is, the effective diffusivity of each species is equal to the thermal diffusivity. It should be noted that in the turbulent zones of the flow where mixing with atmosphere occurs, the turbulent diffusion term for the ith species,

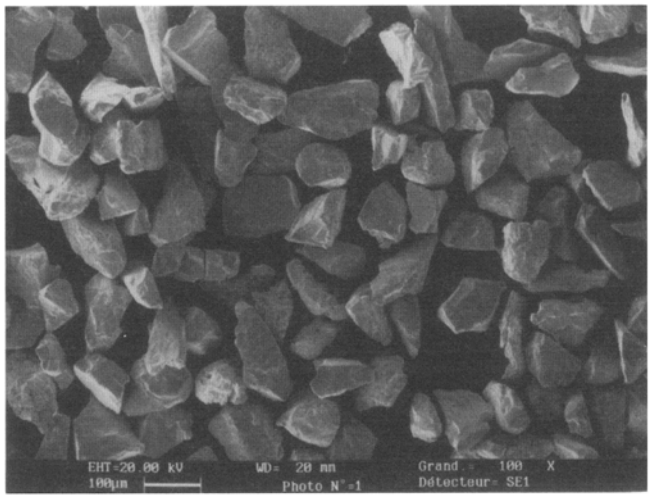

(a)

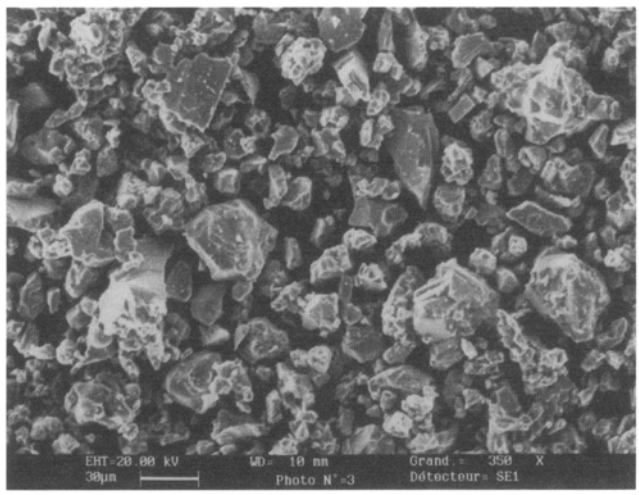

(b)

Fig. 2 Morphology of the sprayed powders. (a) Nb and (b) TiC

$D_{i,t} = \frac{\mu_t}{\rho \cdot Sc_t}$, is far greater than the molecular diffusivity. In addition, as recommended in plasma conditions (Ref 3), the Schmidt turbulent number Sc_t, which compares the momentum diffusivity and the molecular mass diffusivity, was fixed to 0.7.

3.2 Calculation of the Thermodynamic and Transport Properties

Under the conditions of the present study the following gases were present in every point of the calculation grid: Ar + H_2 for the plasma-forming gas, Ar or N_2 for the carrier gas, and Ar or N_2 for the atmosphere. The thermodynamic and transport properties of such a mixture were determined using mixing laws from the properties of pure argon, nitrogen, and argon-hydrogen mixture.

The specific heat and enthalpy of the mixture were expressed as follows:

$$C_P(T) = \sum_i C_{P,i}(T) \cdot m_i \qquad \text{(Eq 2a)}$$

and

$$h(T) = \sum_i h_i(T) \cdot m_i \qquad \text{(Eq 2b)}$$

where $C_{P,i}$, h_i, and m_i are the specific heat, the mass enthalpy, and the mass fraction of species i, respectively.

The viscosity and thermal conductivity were formulated as:

$$\mu(T) = \sum_i \frac{\mu_i}{1 + \sum_{j \neq i} \varphi_{ij} \frac{x_j}{x_i}} \qquad \text{(Eq 3a)}$$

and

$$\kappa(T) = \sum_i \frac{\kappa_i}{1 + \sum_{j \neq i} A_{ij} \frac{x_j}{x_i}} \qquad \text{(Eq 3b)}$$

where x_i is the mole fraction of the species i.

The coefficients φ_{ij} and A_{ij}, which depend on pressure, temperature, and collision integrals, were calculated using the Wilke's approximation (Ref 10):

$$\varphi_{ij} = \frac{1}{\sqrt{8}} \left[1 + \left(\frac{\mu_i}{\mu_j} \right)^{1/2} \left(\frac{M_j}{M_i} \right)^{1/4} \right] \cdot \left[1 + \left(\frac{M_i}{M_j} \right)^{1/2} \right]^{-2} \qquad \text{(Eq 4)}$$

and the Mason and Saxena's approximation (Ref 10):

$$A_{ij} = 1.065\varphi_{ij} \qquad \text{(Eq 5)}$$

where M_i is the molecular weight of species i.

3.3 Geometry and Boundary Conditions

Figure 3 shows the computational domain and the boundary conditions. The symmetries of the domain were not taken into account, because the powder carrier gas tended to deflect the plasma jet, as shown below. A rectangular mesh was used (the axial direction was set to *y*-coordinate) and subdivided in a nonuniform 41 by 42 by 37 grid.

The length of the calculation domain was 100 mm, and its radius was 24 mm, that is, six times the torch radius. At the two inlets of the domain, the torch exit and the powder injector exit, the values of the different variables were fixed. At the torch exit, the following profiles were used for the temperature and the axial component of the velocity, after Chang and Ramshaw (Ref 11):

Table 4 Transport coefficients and source terms used in the conservation equation

φ	Γ_φ	S_φ
1	0	0
u	$\mu_{eff} = \mu + \mu_t$	$-\frac{\partial p}{\partial x} + \rho f_x + \text{div}\left(\mu \frac{\partial V}{\partial x}\right) + \frac{\partial}{\partial x}\left(-\frac{2}{3}\mu \text{div} V\right) + \rho u \text{div} V$
v	μ_{eff}	$-\frac{\partial p}{\partial y} + \rho f_y + \text{div}\left(\mu \frac{\partial V}{\partial y}\right) + \frac{\partial}{\partial y}\left(-\frac{2}{3}\mu \text{div} V\right) + \rho v \text{div} V$
w	μ_{eff}	$-\frac{\partial p}{\partial z} + \rho f_z + \text{div}\left(\mu \frac{\partial V}{\partial z}\right) + \frac{\partial}{\partial z}\left(-\frac{2}{3}\mu \text{div} V\right) + \rho w \text{div} V$
h	$\rho(\kappa/Cp \cdot \rho) + \mu_t/Pr_t$	S_h
X_i	$\rho \cdot D_i + \mu_t/Sc_t$	$\rho \cdot X_i \cdot \text{div} V$
k	μ_{eff}/σ_k	$\rho G - \rho\varepsilon$
ε	$\mu_{eff}/\sigma_\varepsilon$	$\rho\varepsilon/k(C_{\varepsilon 1} G - C_{\varepsilon 2}\varepsilon)$

$$G = \frac{\mu_t}{\rho}\left[2\left(\frac{\partial u}{\partial x}\right)^2 + 2\left(\frac{\partial v}{\partial y}\right)^2 + 2\left(\frac{\partial w}{\partial z}\right)^2 + \left(\frac{\partial u}{\partial y} + \frac{\partial v}{\partial x}\right)^2 + \left(\frac{\partial u}{\partial z} + \frac{\partial w}{\partial x}\right)^2 + \left(\frac{\partial v}{\partial z} + \frac{\partial w}{\partial y}\right)^2\right] \text{ and } \mu_t = \rho C_\mu \frac{k^2}{\varepsilon}$$

$$T = (T_m - T_a)*\left(1 - \left(\frac{r}{R}\right)^{4.5}\right) + T_a \quad \text{(Eq 6)}$$

$$v = v_m*\left(1 - \left(\frac{r}{R}\right)^{2}\right) \quad \text{(Eq 7)}$$

where v_m and T_m are the velocity and temperature of the plasma jet on the torch axis, T_a is the temperature of the anode set to 427 °C, and R is the nozzle radius. v_m and T_m were computed from the enthalpy balance and mass flow rate at the nozzle exit. Although these profiles have been established for a N_2-H_2 plasma jet, their application to an Ar-H_2 plasma jet compares well with the experimental data measured in the laboratory (Ref 12). The nozzle exit was lengthened by a section of larger diameter into which the injector emerged. At the injector exit, the gas velocity profile was set from a former calculation of the flow in the pipe (Ref 13). The remaining part of the entrance plane was considered as a solid wall, as well as the exit plane, which corresponded to the substrate stand-off distance and had a temperature fixed initially at 27 °C. The other boundaries were free, that is, the only condition applying to them was an imposed pressure set equal to atmospheric pressure. The flow at these boundaries was computed so that it could be either inward or outward at different locations on the boundary.

4. Results and Discussion

4.1 Computational Results

The calculations were performed for the operating torch parameters used for TiC deposition.

The effective power dissipated in the gas was 22 kW, and the plasma-forming gas was a mixture of 47 slm argon and 12 slm hydrogen. The plasma jet issued in an atmosphere of argon or nitrogen at 25 °C and atmospheric pressure. Argon or nitrogen was used as the powder carrier gas at a 10 slm flow rate. The 1.7 mm inside diameter (ID) powder injector was located 2.2 mm downstream of the entrance plane and 6 mm off the torch axis.

Figures 4(a) to (c) show the axial profiles of the temperature and velocity of the gas and the mass fraction of the surrounding gas, respectively, when the plasma jet was issued in an argon or nitrogen atmosphere. A maximum temperature of 13,000 °C and a maximum velocity of 1,800 m · s^{-1} were calculated on the jet axis. These values are in reasonable agreement with measurements (Ref 14). Along the centerline, profiles remained

Table 5 Constants of the standard k-ε turbulence model

Constant	Value
C_μ	0.09
$C_{\varepsilon 1}$	1.44
$C_{\varepsilon 2}$	1.00
σ_k	1.92
σ_ε	1.30

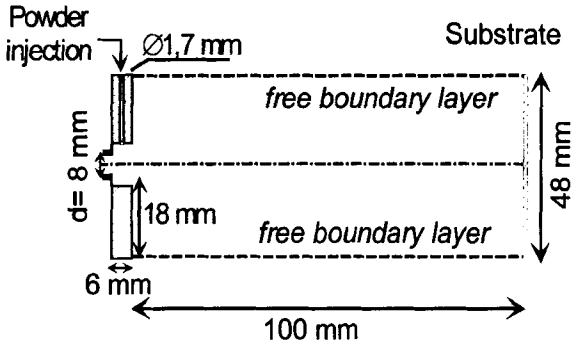

Fig. 3 Calculation domain

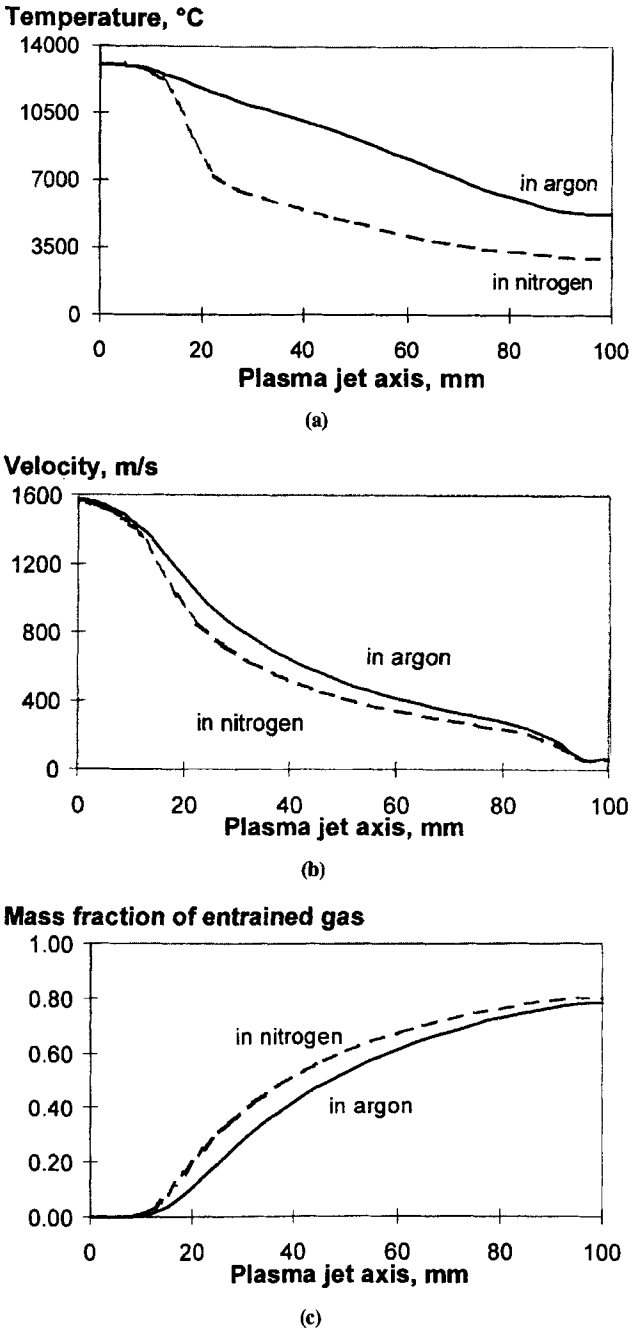

Fig. 4 Gas temperature, gas velocity, and mass fraction of ambient gas along the jet center line

relatively flat for a distance ranging from 10 to 15 mm. This corresponded to the potential core of the jet, where the entrained surrounding gas did not penetrate. Then, the ambient gas was entrained and diffused into the jet, giving rise to a decrease in jet temperature and velocity. If the velocity profiles were nearly the same, temperature decreased far more quickly in the nitrogen atmosphere. This is a consequence of nitrogen dissociation, which occurs at approximately 7200 °C and consumes a part of the plasma enthalpy. In argon, ionization could produce the same effect, but the gas temperature remains below the 15,000 °C required for that process to occur. At a distance of approximately 50 mm from the torch exit, the mass fraction of the ambient gas exceeds 50% in the gas flow; that is, the jet is fully turbulent. At the substrate stand-off distance, the mass fraction of the entrained gas on the jet centerline grows to 80%; the corresponding temperature is around 5700 °C in the argon atmosphere and 2000 °C lower in the nitrogen atmosphere. It should be noticed that cryogenic cooling of the substrate was not taken into account in the computations. During the experiments, the cold gas issuing from the cryogenic device mixed with the plasma jet and efficiently cooled it close to the substrate.

For argon and nitrogen atmospheres respectively, Fig. 5 shows the isovalues of temperature, and Fig. 6 shows the isovalues of the mass fraction of the ambient gas. The plasma jet issuing from the torch is deflected by the powder carrier gas with a maximum deviation of 2°. The temperature isolines are restricted in the region of injection due to mixing with cold gas. The penetration and spreading of the transverse cold jet depend strongly on the ratio of the relative momentum of both jets. This can be expressed, as proposed by Njah (Ref 15), by:

$$Rm = \frac{Q_{m,inj}/S_{inj}}{Q_{m,f}/S_f} \quad \text{(Eq 8)}$$

where Q_m is the mass flow rate, S is the surface of the inlet, and subscripts "inj" and "f" refer to the injected gas and the plasma flow, respectively. Under the conditions of this study, $Rm = 4.4$, which seems to be sufficiently high for the carrier gas to produce a deviation of the plasma jet (Fig. 5 and 6). A stronger entrainment of ambient gas is noticeable when nitrogen is used; the predicted maximum value of turbulent kinetic energy is in the order of $9 \cdot 10^4$ m^2s^{-2} in that case, compared to $7.5 \cdot 10^4$ m^2s^{-2} when spraying in argon. Because nitrogen is less dense than argon, its turbulent diffusion coefficient is higher than that of argon.

As already shown in Fig. 4b, the isovalues of velocity in the axial plane containing the injector, Fig. 7, show little difference in the different atmospheres.

4.2 Coating Properties

Table 6 summarizes deposition efficiency, adhesion strength, Vickers microhardness, roughness, and chemical analysis of the niobium and titanium carbide coatings.

The average thickness of the coatings was 50 μm for niobium and 120 μm for TiC. The niobium coatings were very thin, and their adhesion was poor. Previous experiments (Ref 16) have already shown that a controlled atmosphere and an external powder injection always lead to detachment of the niobium coating from the substrate. With an internal powder injection, well-bonded niobium coatings can be produced under controlled atmosphere. This can be explained by more efficient heating of the powder and longer residence time in the hot zones of the plasma jet resulting in a chemical reaction between the niobium and the H_2 plasma-forming gas that causes the formation of NbH_x. However, after heat treatment, the latter disappears and the coating peels off (Ref 16).

Optical micrographs were used to evaluate coating thickness and to examine their microstructures (Fig. 8, Table 6).

Coatings sprayed under argon or nitrogen atmosphere exhibited the same lamellar microstructure and grain size (Fig. 8). No secondary phase such as a nitride was detected before and after heat treatment by optical and scanning electron microscopy (SEM) observations. An energy dispersive x-ray analysis has revealed no nitrogen trace in niobium and TiC coatings sprayed under nitrogen atmosphere; the coatings contained less than 1% of nitrogen atoms (which is the detection threshold of lighter elements with this technique).

For TiC powder, the deposition efficiency was slightly higher in the argon atmosphere. As shown by the mathematical predictions, the length and diameter of the plasma jet were higher in the argon atmosphere than in the nitrogen atmosphere. This resulted in a more uniform heating of the particles in the spray jet and, thus, in a higher deposition efficiency.

For each coating, the tensile adhesion test led to failure at the coating-substrate interface. The adhesion strengths were similar

Table 6 Coatings properties

	Nb		TiC	
Properties	**Ar**	**N_2**	**Ar**	**N_2**
Deposition efficiency, %	...	...	59 (±3)	54 (±3)
Adhesion strength, MPa				
As-sprayed	...	...	5.3 (±0.1)	3.9 (±0.4)
After 1250 °C, 10 h	...	...	6.0 (±0.4)	4.8 (±0.6)
Vickers microhardness	160 ± 15	500 ± 40	1275 ± 85	1300 ± 220
Roughness				
R_a, μm	12 (±1)	12 (±1)	9 (±1)	9 (±1)
R_t, μm	93 (±13)	92 (±9)	66 (±6)	67 (±5)
Chemical content, wt%				
C	0.008 (±0.002)	0.008 (±0.002)	20.3 (±0.4)	19.6 (±0.3)
O	0.16 (±0.02)	0.15 (±0.02)	0.17 (±0.03)	0.15 (±0.03)
N	0.052 (±0.002)	1.04 (±0.02)	0.071 (±0.007)	0.380 (±0.008)
C/Ti	...	...	1.01 (±0.03)	0.97 (±0.02)

whatever the nature of the surrounding gas. Adhesion tests applied to other coating materials, not presented in the paper, confirmed this result. The heat treatment (1250 °C for 10 h) did not substantially improve the adhesive strength of the TiC deposits. Carbon diffusion from the graphite substrate to the TiC coating was low, and so the substrate-coating interface was not really reinforced.

Microhardness measurements did not allow for discrimination of the TiC coatings sprayed under argon and nitrogen atmospheres. Nevertheless, niobium coatings obtained with a nitrogen atmosphere were harder, possibly because of diffusion of nitrogen atoms in the coating.

Roughness tests did not show any difference between coatings due to the nature of the surrounding gas. Because of the low thickness of the niobium coatings, their roughness was similar to that of the graphite substrates (R_a = 11 μm, R_t = 85 μm).

Niobium powder and coatings have been characterized by Raman spectroscopy. The Raman lines of N_2 and O_2 were detected

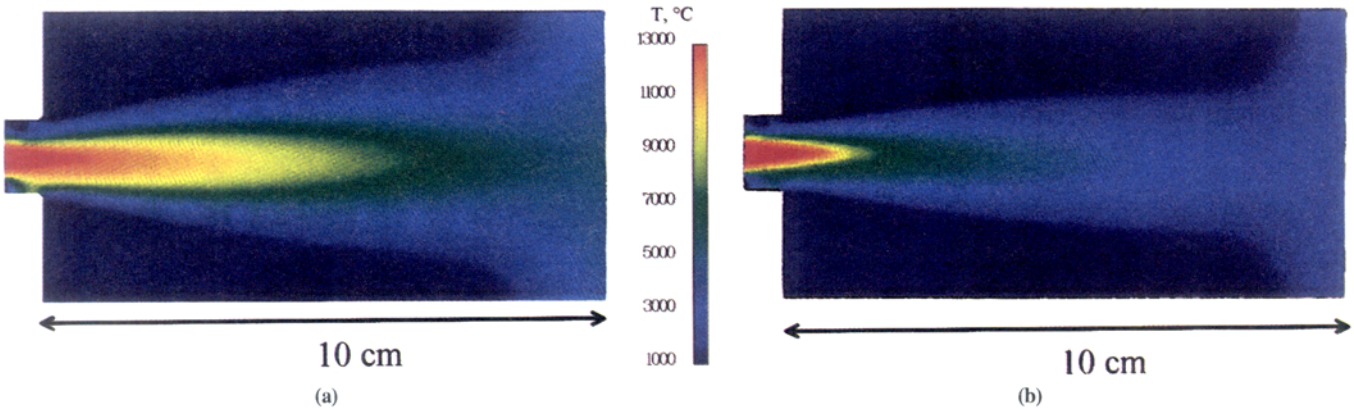

Fig. 5 Isovalues of gas temperature in the injection plane for argon and nitrogen atmosphere. (a) argon. (b) nitrogen

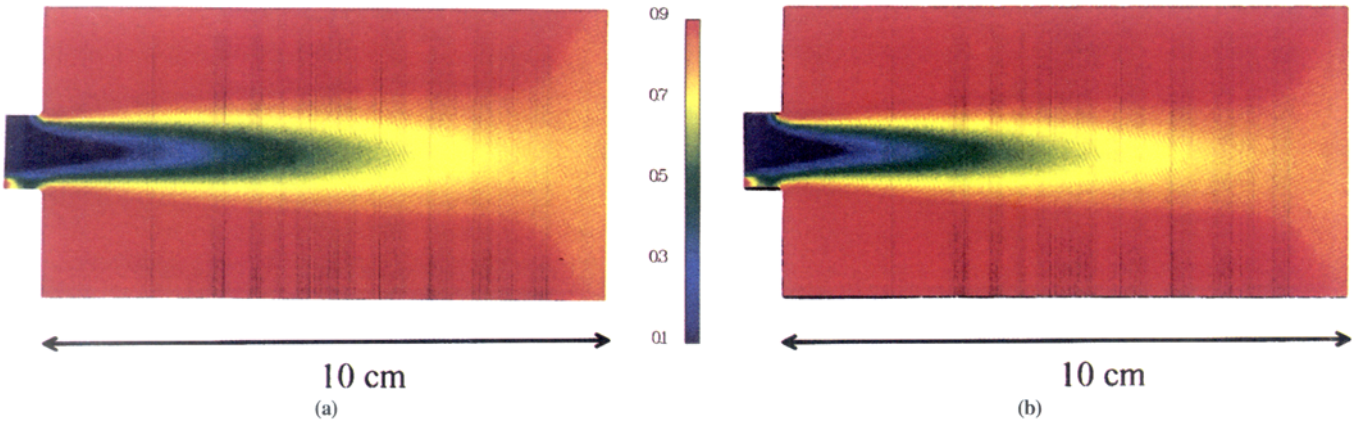

Fig. 6 Isovalues of mass fraction of atmospheric gas in the injection plane in argon and nitrogen atmosphere. (a) argon. (b) nitrogen

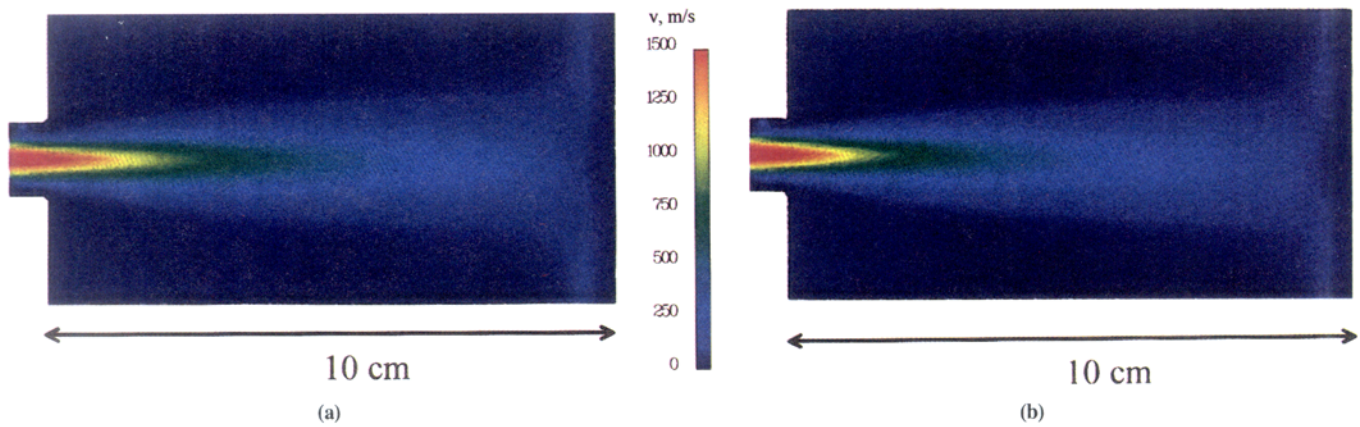

Fig. 7 Isovalues of gas velocity in the injection plane in argon and nitrogen atmosphere. (a) argon. (b) nitrogen

at 2326 ± 5 cm^{-1} and at 1553 ± 5 cm^{-1}, respectively. The ratio $\beta = I_{N_2}/I_{O_2}$, where I is the peak intensity, is presented in Table 7. This shows that the niobium coating sprayed under nitrogen atmosphere contained more nitrogen atoms than the coating sprayed under argon. But this analysis did not allow for knowledge of the chemical bond nature between nitrogen and niobium atoms.

The C/Ti atomic ratio can be formulated as:

$$x = \frac{C}{Ti} = \frac{M_{Ti}}{M_C} \times \frac{C\%}{100 - C\%}$$

where M_{Ti} is the molecular weight of titanium, M_C is the molecular weight of carbon, and C% is the total carbon content in the TiC coating (wt%), determined by the Rosemount analyzer.

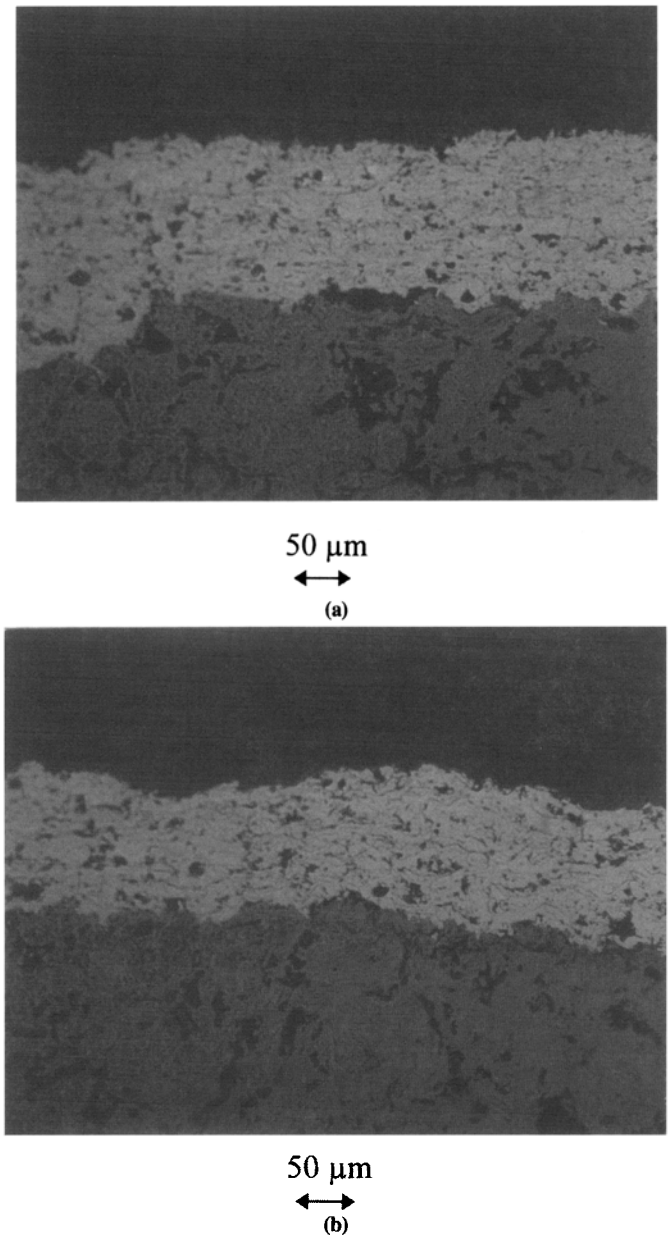

Fig. 8 Metallographic cross sections of as-sprayed TiC coatings

The C/Ti atomic ratio in the initial TiC powder was 0.95 ± 0.03. After spraying, this ratio remained approximately constant. Therefore, no TiC decarburization occurred during spraying under either argon or nitrogen atmospheres.

Spraying under nitrogen atmosphere resulted in a nitrogen content increase of 1% for niobium coatings and 0.3% for TiC coatings. These results indicate some interaction between the powder and the surrounding gas during the process.

Figure 9 shows the x-ray diffraction patterns of the niobium and TiC coatings before and after heat treatment. The number and the position of peaks are the same for all TiC coatings. Therefore, according to this analysis, no secondary phase has appeared in the TiC coatings. Figure 9 shows that the peaks of niobium coating sprayed in nitrogen atmosphere are shifted toward the little 2θ angles compared to the coatings sprayed in argon. This difference can be explained by a nitrogen atom insertion in the octahedral and tetrahedral sites of niobium. The Nb_2C phase was detected in the niobium coating after 10 h at 1250 °C. This was explained by the carbon diffusion from the graphite substrate to the coating. After heat treatment, all the peaks were narrower and more intense because of enhanced crystallization and stress relaxation. Nevertheless, no nitride phase has been detected by x-ray diffraction, even for the niobium coatings, which contained approximately 1% nitrogen.

4.3 Discussion

The particles entrained in the plasma jet flowing in the N_2 reactive atmosphere can be subjected to interactions with the surrounding gas in flight or after impact on the substrate. However, in this study, the cryogenic cooling of the substrate most likely prevented reactions after the splats were formed.

The experimental results showed that the N_2 content was more important in the niobium coatings than in the TiC coatings. Approximations of particle melting time and time of flight were calculated to determine if nitrogen absorption in flight could explain this difference. N_2 was assumed to diffuse in the liquid particles because temperatures involved outside of the potential jet core were inferior to the dissociation temperature of nitrogen.

A lumped-heat capacity model was used for the heating of particles, as justified by the low value of the Biot number, *Bi*

Table 7 Raman spectroscopy results

	Niobium		
	Powder	Coating (Ar atmosphere)	Coating (N_2 atmosphere)
$\beta = I_{N_2}/I_{O_2}$	3.9 (±0.2)	3.6 (±0.2)	3.9 (±0.2)

Table 8 Estimated residence time of particles when the plasma jet issued in a nitrogen atmosphere

	Nb	TiC
Mass density, kg · m^{-3}	8570	4930
Particle mean diameter, μm	100	25
Biot number, *Bi*, at T_f = 4200 °C	0.03	0.07
Time necessary to reach the melting temperature, ms	0.075	0.006
Residence time, ms	2	1

(Ref 17). Assuming that the heat transfer to particles is essentially conductive, this number can be written:

$$Bi = \frac{\bar{\kappa}_f}{\kappa_p} = \frac{1}{\kappa_p}\left(\frac{1}{T_f - T_p}\int_{T_p}^{T_f} \kappa(T)dT\right) \quad \text{(Eq 9)}$$

where $\bar{\kappa}_f$ is the mean thermal conductivity of the gas integrated between particle temperature T_p and temperature of the flow far from the particle T_f, and κ_p is the thermal conductivity of material at temperature T_p. When $Bi < 0.1$, internal gradients are negligible, and the temperature of the particle can be assumed to be uniform (Ref 17).

For both materials used in this study, the Biot number was less than 0.1 when assuming a mean temperature of the gas equal to 4200 °C, resulting in a value of $\bar{\kappa}_f$ of 1.5 $W \cdot m^{-1} \cdot °C^{-1}$ (Table 8). Thus, the approximation of a uniform temperature in the particle can be considered as valid.

The heat required for a particle to reach melting temperature is:

$$\Delta H_{me} = \frac{\pi d_P^3}{6}\rho_p C_{P,p}(T_{me} - 300) = h\pi d_P^2(T_f - T_p)t_{me} \quad \text{(Eq 10)}$$

where T_{me} is the melting temperature of the material, h is the heat transfer coefficient, and t_{me} is the time necessary to reach the melting temperature from an initial temperature of 25 °C. The heat transfer coefficient is calculated from the Nusselt number $Nu = hd_p/\kappa_f$, which has a value of 2 when heat transfer occurs only by conduction (Ref 18). Therefore, t_{me} can be expressed as:

$$t_{me} = \frac{d_P^2 \rho_p C_{P,p}}{12\bar{\kappa}_f}\frac{T_{me} - 300}{T_f - T_p} \quad \text{(Eq 11)}$$

Table 8 shows the values of t_{me} calculated for niobium and TiC particles assuming a temperature difference $(T_f - T_p)$ of 4000 °C · t_{me} is less than 0.1 ms, which approximates the residence time of the particles in the potential core. Therefore, particles are at least superficially melted when exiting the potential core where the environmental gas has not penetrated and can be subjected to nitridation.

To determine the total residence time, particles were assumed to follow a trajectory making an angle of 4° with the torch centerline. The equation of motion of the particle can be expressed in the following simplified equation by assuming that the only force acting on the particle is the drag force and that the flow around the spherical particle is in the creeping flow region (Ref 18):

$$\frac{dv_p}{dt} = \frac{18\mu_f}{\rho_p d_p^2}(v_f - v_p) \quad \text{(Eq 12)}$$

where v_p and v_f are the velocity of the particle and plasma jet along the jet axis.

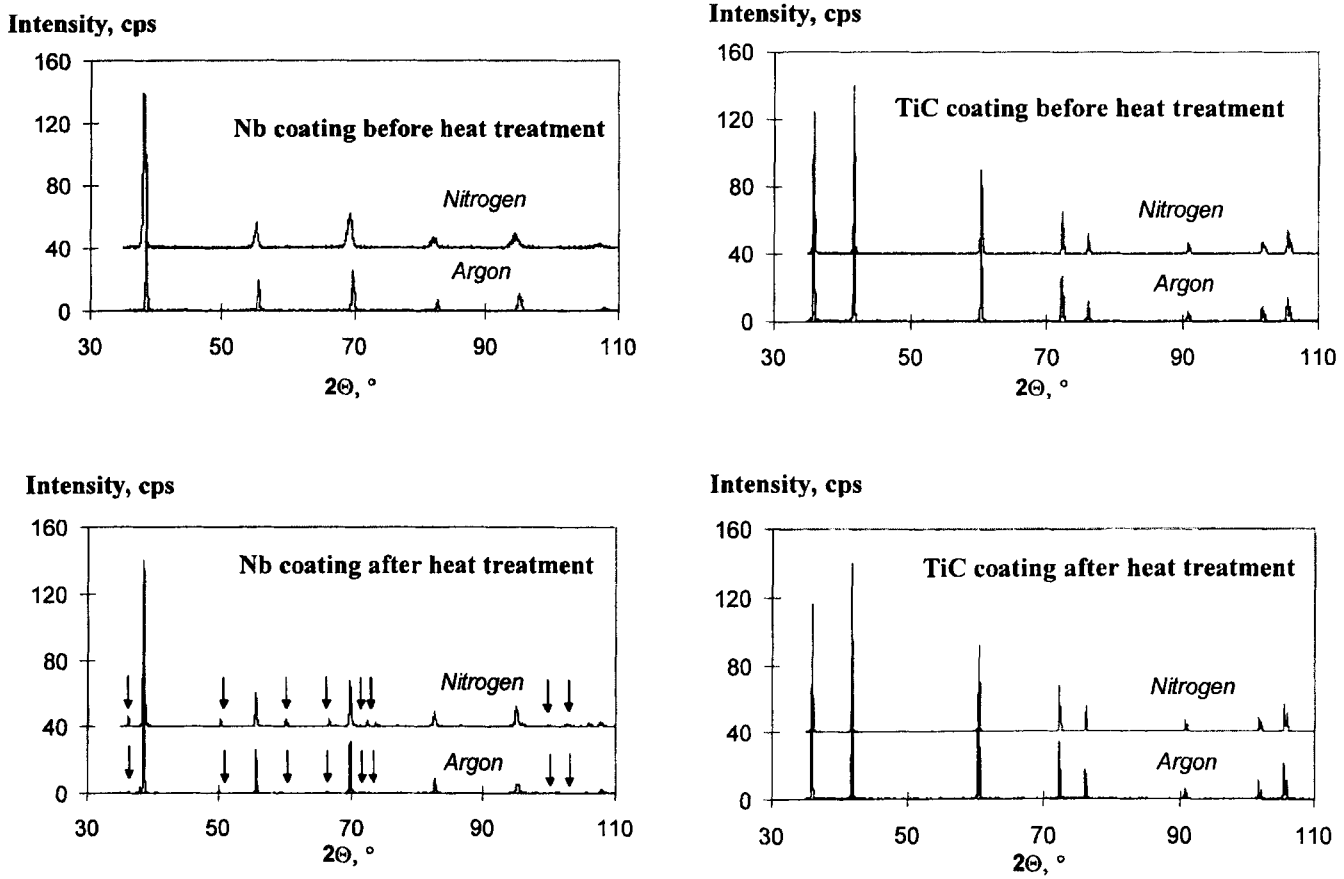

Fig. 9 X-ray diffraction pattern for niobium and TiC coatings. Arrows indicate Nb_2C peaks.

The integration of Eq 12 from time $t = 0$ to t, yields the following equation if the gas viscosity is assumed constant:

$$v_p(t) = v_f(t) - (v_{f,0} - v_{p,0}) \exp\left(-\frac{18\mu_f}{\rho_p d_p^2} t\right) \quad \text{(Eq 13)}$$

where $v_{f,0}$ and $v_{p,0}$ refer to fluid and particle velocity values at $t = 0$, respectively.

The residence time t_r of the particle in the plasma jet can be computed from this equation as the sum of time steps, Δt, during which particle velocity is assumed to be constant. Under these assumptions, the residence time of the niobium particles was found to be higher than the residence time of the titanium carbide particles. Moreover, particles were found to be at least partially liquid in the zones where nitrogen is present (Table 8). As the values of the diffusion coefficient in liquids are almost all approximately of the same order of magnitude, the difference in residence times can explain the higher nitrogen content of niobium coatings.

5. Conclusions

In an inert plasma spray process, the use of a nitrogen atmosphere instead of an argon atmosphere results in coatings with quite similar properties. The nitrogen content of the niobium and titanium carbide coatings analyzed in this paper was at most 1%. This result was confirmed with other ceramic and metal coatings (Ref 19). The diffusion of nitrogen seemed to occur in the molten droplets in flight, with the cryogenic cooling of the substrate by liquid nitrogen jets preventing the reactions after impact of the droplets onto the substrate. Gas flow fields were computed in nitrogen and argon atmospheres. The predictions confirm the small differences observed for coating properties.

Under the conditions of the present study, the replacement of argon by nitrogen as an inert atmosphere seems feasible, thus reducing costs by approximately 30%.

References

1. J.R. Fincke, W.D. Swank, and D.C. Haggard, Plasma Spraying of Alumina: Plasma and Particle Flow Fields, *Plasma Chem. Plasma Process.*, Vol 13 (No. 4), 1993, p 579-600
2. P. Roumilhac, A. Vardelle, M. Vardelle, J.F. Coudert, and P. Fauchais, Comparison of Ar-H_2 and Ar-He Plasma Jets Produced by a D.C. Plasma Torch Working either in Air or in a Controlled Atmosphere Chamber at Atmospheric Pressure, *Proc. of the 12th Int. Thermal Spray Conf., 4-9 June 1989* (London), I.A. Bucklow, Ed., Abington International, 1989, p 65-69
3. P. Proulx, "Modélisation Mathématique des Ecoulements Plasma-Particules," Ph.D. thesis, Sherbrooke University, Quebec, Canada, July 1987 (in French)
4. A. Vardelle, P. Fauchais, and N.J. Themelis, Oxidation of Metal Droplets in Plasma Sprays, *Advances in Thermal Spray Science and Technology*, C.C. Berndt and S. Sampath, Ed., ASM International, 1995, p 175-181
5. A. Vardelle, N.J. Themelis, B. Dussoubs, M. Vardelle, and P. Fauchais, Transport and Chemical Rate Phenomena in Plasma Sprays, *High Temp. Mater. Process.*, Vol 1 (No. 3), 1997, p 295-314
6. J.D. Mattei and O. Simonin, Estet software v. 3.1 Theoretical Handbook, Vol 1, Physical Modeling, EDF Report No. HE 44/92.38B, 1992, EDF-LNH (in French)
7. J.D. Mattei and O. Simonin, Estet software v. 3.1 Technical Handbook, Descriptif Informatique du Code ESTET, Version 3.1, EDF Report No. HE 44/93.20, 1992 (in French)
8. B.E. Launder and D.B. Spalding, The Numerical Computation of Turbulent Flows, *Computer Methods in Applied Mechanics and Engineering*, Vol 3, 1974, p 269-289
9. B.E. Launder and B.I. Sharma, Application of the Energy-Dissipation Model of Turbulence to the Calculation of Flow Near a Spinning Disc, *Letters in Heat and Mass Transfer*, Vol 1, 1974, p 131-138
10. R.C. Reid and T.K. Sherwood, *The Properties of Gases and Liquids*, 2nd ed., McGraw Hill, 1966, p 420-423, 483-486
11. C.H. Chang and J.D. Ramshaw, Modeling of Non-Equilibrium Effects in a High-Velocity Nitrogen-Hydrogen Plasma Jet, *Plasma Chem. Plasma Proc.*, Vol 16, 1996, p 5S-17S
12. J.F. Coudert, M.P. Planche, and P. Fauchais, Velocity Measurement of D.C. Plasma Jets Based on Arc Root Fluctuations, Spray Torch, *Plasma Chem. Plasma Proc.*, Vol 15 (No. 1), 1995, p 47-70
13. B. Dussoubs, A. Vardelle, K.-I. Li, M. Vardelle, and P. Fauchais, Injection and Trajectories of Particles in D.C. Plasma Spray Processes, in *Proc. of the 12th Int. Symp. on Plasma Chemistry*, J.V. Heberlein, D.W. Ernie, and J.T. Roberts, Ed., University of Minnesota, Minneapolis MN, 1992, p 1343-1348
14. J.F. Coudert, M.P. Planche, and P. Fauchais, Velocity Measurement of D.C. Plasma Jets Based on Arc Root Fluctuations, *Plasma Chem. Plasma Proc.*, Vol 15 (No. 1), 1995 p 45-70
15. Z. Njah, J. Mostaghimi, and M.I. Boulos, Mathematical Modeling of the 3-D Mixing in an Induction Plasma Reactor, *Int. J. of Heat Mass Transfer*, Vol 36 (No. 16), 1993, p 3909-3919
16. M. Berardo, Controlled Atmosphere and Temperature Plasma Spraying Unit, CEA Internal Report, CEA-Institute of Technical Research and Industrial Development-CEA/Valrho, 1988 (in French)
17. J.F. Sacadura, *Initiation Aux Transferts Thermiques*, Tech. et Doc, Lavoisier, 1993, p 45-48 (in French)
18. D.R. Poirier and G.K. Geiger, Transport Phenomena in Materials Processing, TMS, 1994, p 288-292
19. M. Leylavergne, CEA Internal Report, CEA-Institute of Technical Research and Industrial Development-CEA/Valrho, 1988 (in French)